Materials Chemistry and Physics 276 (2022) 125397

Contents lists available at ScienceDirect

Materials Chemistry and Physics

journal homepage: www.elsevier.com/locate/matchemphys

Corrosion behavior of AlCuFeMn alloy in aqueous sodium chloride solution

A. Dutta [a], T. Sivaji [a], M. Ghosh [b], R. Fernandes [c], P.S. De [a,*], D. Nayak [a,d], R. Sharma [a]

[a] School of Minerals, Metallurgical and Materials Engineering, Indian Institute of Technology Bhubaneswar, India
[b] Materials Engineering Division, CSIR-National Metallurgical Laboratory, Jamshedpur, India
[c] Department of Physics and Electronics, Christ University, Bangalore, India
[d] CSIR-Institute of Minerals & Materials Technology, Bhubaneswar, India

HIGHLIGHTS

- As cast AlCuFeMn alloy comprises of FCC and BCC phases only.
- Corrosion rate in 3.5 wt% NaCl solution of as-cast alloy comparable to CoCrFeMnNi alloy.
- Surface oxidized alloy corrosion rate is comparable to AISI 304.
- The as-cast alloy surface revealed metallic as well as oxidized elemental states.
- In oxidized alloy surface chiefly oxidized elemental states are present.

ARTICLE INFO

Keywords:
Medium entropy alloy
EIS
XPS
Pitting corrosion

ABSTRACT

Medium Entropy Alloy AlCuFeMn possesses high room temperature strength and oxidation endurance. In present work, the aqueous corrosion resistance of the as-cast as well as low temperature oxidized AlCuFeMn alloy in 3.5 wt% NaCl solution, is explored. Equimolar proportions of high purity copper, manganese, iron, and aluminum were arc melted and cast in a copper mold. The alloy primarily consists of a face-centered cubic and a body-centered cubic phase. Potentiodynamic polarization tests on the alloy after low temperature surface oxidation reveal an aqueous corrosion resistance comparable to AISI 304 steel and CoCrFeMnNi high entropy alloy. The X-ray photoelectron spectroscopic studies confirmed that the free surface in the as-cast alloy is in partially oxidized state. The same completely oxidizes after low-temperature surface oxidation. Such low temperature surface oxidation improves pitting corrosion resistance in AlCuFeMn alloy due to increased metal/oxide layer resistance. The electrochemical impedance spectroscopy tests coupled with microscopy confirmed that the principal corrosion mechanisms in the alloy are of the uniform and pitting type. The energy dispersive spectroscopy experiments indicate that a copper oxide enriched layer is formed on the surface oxidized specimen during corrosion.

1. Introduction

The quest for materials with high strength to weight ratio and corrosion resistance is leading researchers to investigate a broad realm ranging from metals and alloys to composite materials. Many equimolar and near-equimolar high/medium entropy alloys (HEAs/MHEAs) possess, excellent mechanical property [1,2] and a corrosion resistance similar to or better than stainless steels [3–5]. However, the bulk of HEA/MHEA alloy compositions proposed in literature involve 3d elements, of high density. Therefore, incorporating light weight elements like aluminum and or titanium in existing HEA/MHEA alloy framework is of substantial interest. Recently, Roy et al. reported the structure and mechanical properties of annealed equimolar AlCuFeMn alloy (773 K for 80 h) [6]. The alloy exhibits yield strength of ~1000 MPa which is significantly high compared to many commercial structural alloys. Again, oxidation resistance of the AlCuFeMn alloy is similar to Inconel and or stainless steel [7]. However, aqueous corrosion resistance of cast AlCuFeMn alloy is not reported in literature. Therefore, present work investigates the aqueous corrosion resistance of an as-cast AlCuFeMn alloy in 3.5 wt% aqueous NaCl solution in details.

Again, aluminum/titanium dissolved in an alloy forms surface oxides rendering high oxidation resistance to the alloys [8]. Thus, aluminum in

* Corresponding author.
E-mail address: parthasarathi.de@iitbbs.ac.in (P.S. De).

https://doi.org/10.1016/j.matchemphys.2021.125397
Received 13 October 2019; Received in revised form 2 October 2021; Accepted 30 October 2021
Available online 1 November 2021
0254-0584/

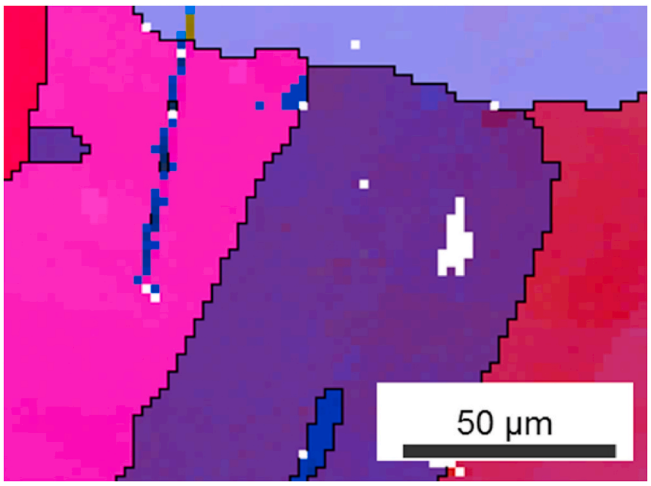

Fig. 1. Euler contrast map of as-cast AlCuFeMn alloy cross-section showing elongated grains (only FCC phase mapped). The white regions are unresolved. The thick black lines are high angle grain boundaries.

iron improves scaling resistance with ~12% aluminum sufficient to resist oxidation at 1300 °C [8]. But, such iron aluminides are susceptible to environmental degradation due to hydrogen formed by the reaction between moisture and aluminum atoms [9,10] and possess a poor aqueous corrosion resistance [11]. Therefore, additional element substitution i.e. copper and manganese, in the binary aluminum-iron system to form HEA/MHEA alloys and corresponding reduction in aluminum chemical potential is expected to improve aqueous corrosion resistance without affecting strength and endurance to oxidation. Therefore, the present study specifically investigates the role of each element on the aqueous corrosion resistance of as-cast AlCuFeMn alloy using potentiodynamic polarization, electrochemical impedance spectroscopy (EIS), and x-ray photoelectron spectroscopy (XPS) techniques. The following section discusses the experimental details of this work in more detail.

2. Experimental procedure

High purity metal wires of iron, aluminum, copper (all >99.99%), and manganese granules (purity >99.95%) were mixed in equimolar proportions and arc-melted in a water-cooled copper mold in an ultra-high purity argon atmosphere to form an alloy button. The as-cast button was flipped and re-melted six times and the top 1 mm of the final sample removed to ensure homogeneous composition. The bulk composition was then evaluated using energy dispersive spectroscopy. Subsequently, a test specimen of surface area 41.0 mm^2 was sectioned from the as-cast alloy button (**Sample A**) and cold-mounted in epoxy resin. The exposed surface was polished and etched using Glyceregia (2 ml Glycerine + 3 ml HCl + 1 ml HNO_3) for 30 s. The microstructure of

Table 1
SEM-EDS compositional analysis of Regions 1 & 2 of AlCuFeMn alloy (in atom %) and AISI 304 (in weight %).

AlCuFeMn alloy				
	Al	**Cu**	**Fe**	**Mn**
Average Composition	24.3 ± 1.3	26.7 ± 4.3	24.5 ± 2.9	24.4 ± 1.3
Region 1 (Fe Rich)	24.6 ± 1.2	23.7 ± 1.8	26.5 ± 1.5	25.0 ± 1.1
Region 2 (Cu Rich)	23.9 ± 1.2	30.3 ± 3.5	22.2 ± 2.2	23.7 ± 1.1

AISI 304							
Cr	**Fe**	**Mn**	**Ni**	**Si**	**Cu**	**S**	**P**
19.2 ± 0.2	71.3 ± 0.2	0.94 ± 0.1	7.9 ± 0.2	0.3 ± 0.03	0.54 ± 0.05	0.02 ± 0.0	0.01 ± 0.0

the etched specimen was characterized using Field Emission Scanning Electron Microscope (FE-SEM) and energy dispersive spectroscopy (EDS). The phase identification was done in Transmission Electron Microscopy (TEM), complemented by Electron Backscattered Diffraction (EBSD), and powder X-ray diffraction (XRD) where CuKα radiation at 40 kV and 40 mA was used. For EBSD investigation, the crystal structure and composition information for AlCuFeMn alloy obtained from TEM results, EDS experiments, XRD data of current experiments, and the work of Roy et al. [6] were used. The crystal structure data generated was applied to simulate Kikuchi patterns for three out of total four phases identified. This was subsequently employed during EBSD

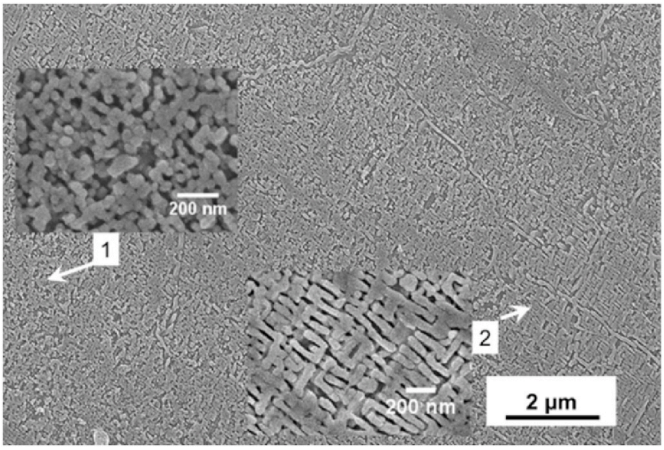

Fig. 3. Morphology of the alloy after glyceregia etching. Inset shows Region 1 with cuboidal structures of size ~25–50 nm and Region 2 with threaded interweaved structure.

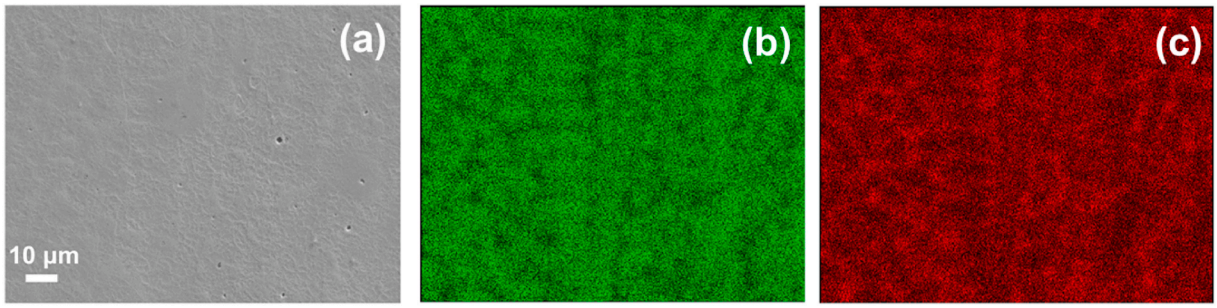

Fig. 2. (a) Secondary electron image of the etched dendritic surface (b) Iron and (b) Copper segregation. (Note: No marker bar is provided in (b) or (c) as they correspond to image (a)). Aluminum and manganese content is similar in both regions.

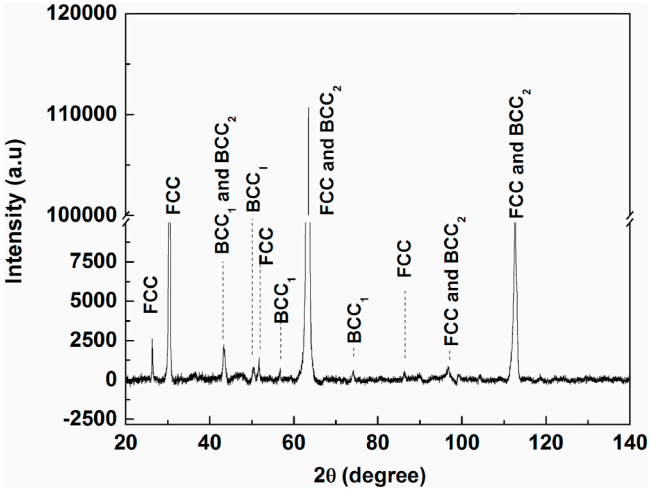

Fig. 4. XRD Spectra of as-cast AlCuFeMn medium entropy alloy using CuKα radiation at 40 kV and 40 mA.

mapping of samples where experimental Kikuchi patterns were matched with at least eleven bands (twelve maximum), to differentiate between the individual phases. The EBSD mapping step size was varied between 2 μm and 0.06 μm, where gross microstructure was mapped using coarse steps while detailed phase identification was done using fine step size.

An additional surface oxidized as-cast specimen (exposed to air at 473 K for 5 h) was prepared (designated as **Sample B)** to study the effect of oxidation on corrosion behavior. To understand the reason behind underlying corrosion behavior, both the as-cast and the surface oxidized specimens **(Sample A** and **B**) were investigated using XPS (PHI 5000 VersaProbe II) equipped with a monochromatic Al Kα (1486.6 eV) X-ray source and a hemispherical analyzer. Electrical charge compensation was applied to perform the XPS analysis where all the binding energies (B.E.) were referenced to the C1 s peak at 284.8 eV.

Subsequently, room temperature corrosion behavior of both **Sample A** and **B** and a typical AISI 304 material in 3.5 wt% aqueous NaCl solution (de-aerated using Nitrogen) were investigated using potentiodynamic polarization and EIS. A three-electrode flat cell with the specimen as a working electrode, platinum as a counter electrode and a saturated calomel reference electrode (SCE, E = 0.2415V_{SHE}) was used. Prior to the potentiodynamic polarization and EIS tests, the OCP value was recorded for 1 h to ensure steady-state potential. Potentiodynamic polarization measurements were started at the Open-Circuit Potential (OCP) value and scanned ± 0.5 V with respect to OCP at a scan rate of 0.17 mV/s in accordance with ASTM G61 [12]. The EIS was performed over a frequency range of 10^5 to 10^{-2} Hz, with a sinusoidal signal of 5 mV amplitude and OCP as the mean value [13]. The EIS data were fitted for electrical equivalent circuit using NOVA™ software. Later, the corroded AlCuFeMn alloy samples were sectioned and examined using EDS, to understand the corrosion phenomena. The following section discusses the results in detail.

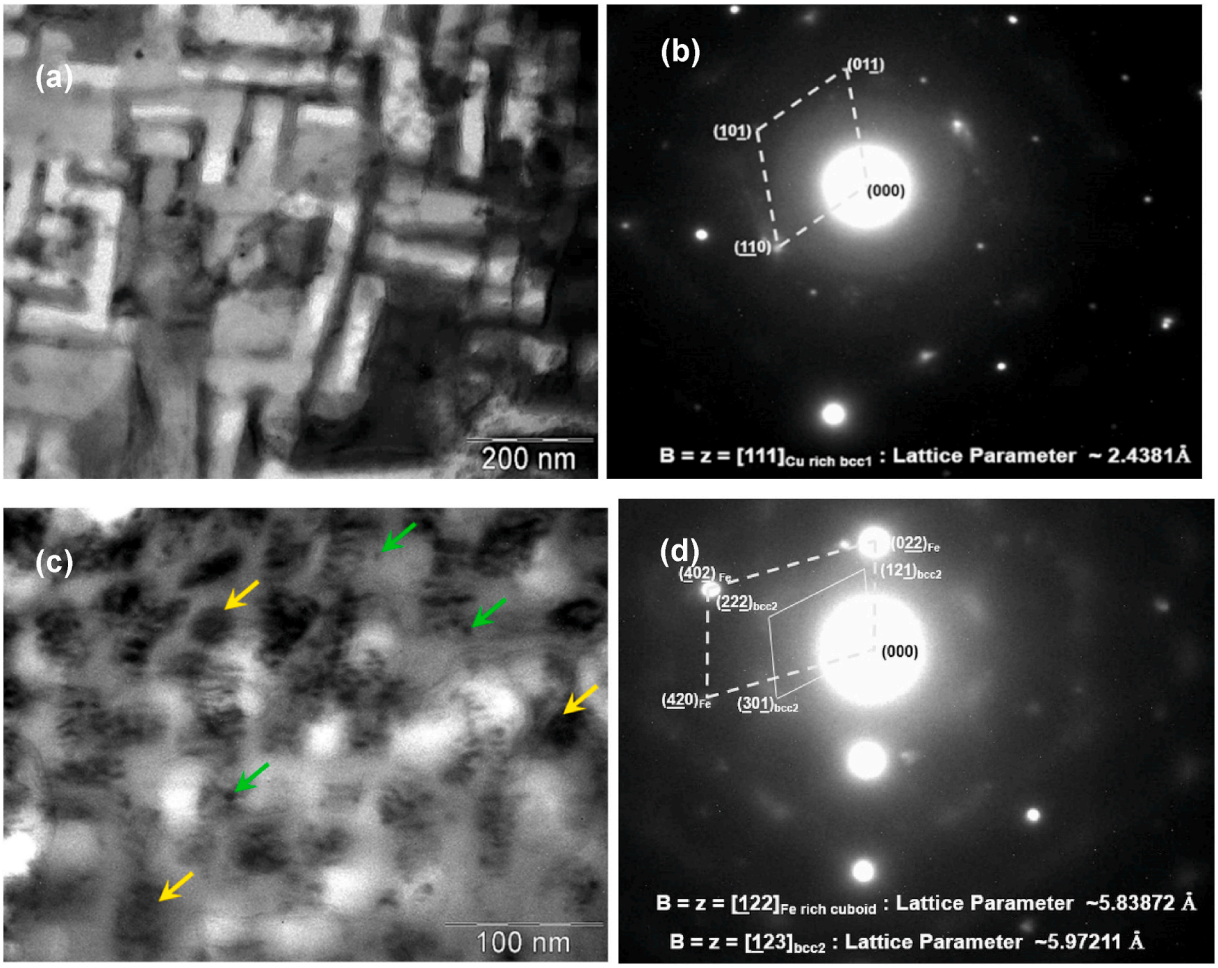

Fig. 5. (a) Bright field image of Region-2 showing the BCC_2 phase with interlaced structure, (b) The Selected Area Diffraction pattern corresponding to Figs. 5(a), (c) The bright field image of Region-1 where green arrows correspond to the BCC phase while yellow arrows correspond to FCC phase, and (d) The SAD pattern corresponding to Fig. 5(c). (For interpretation of the references to colour in this figure legend, the reader is referred to the Web version of this article.)

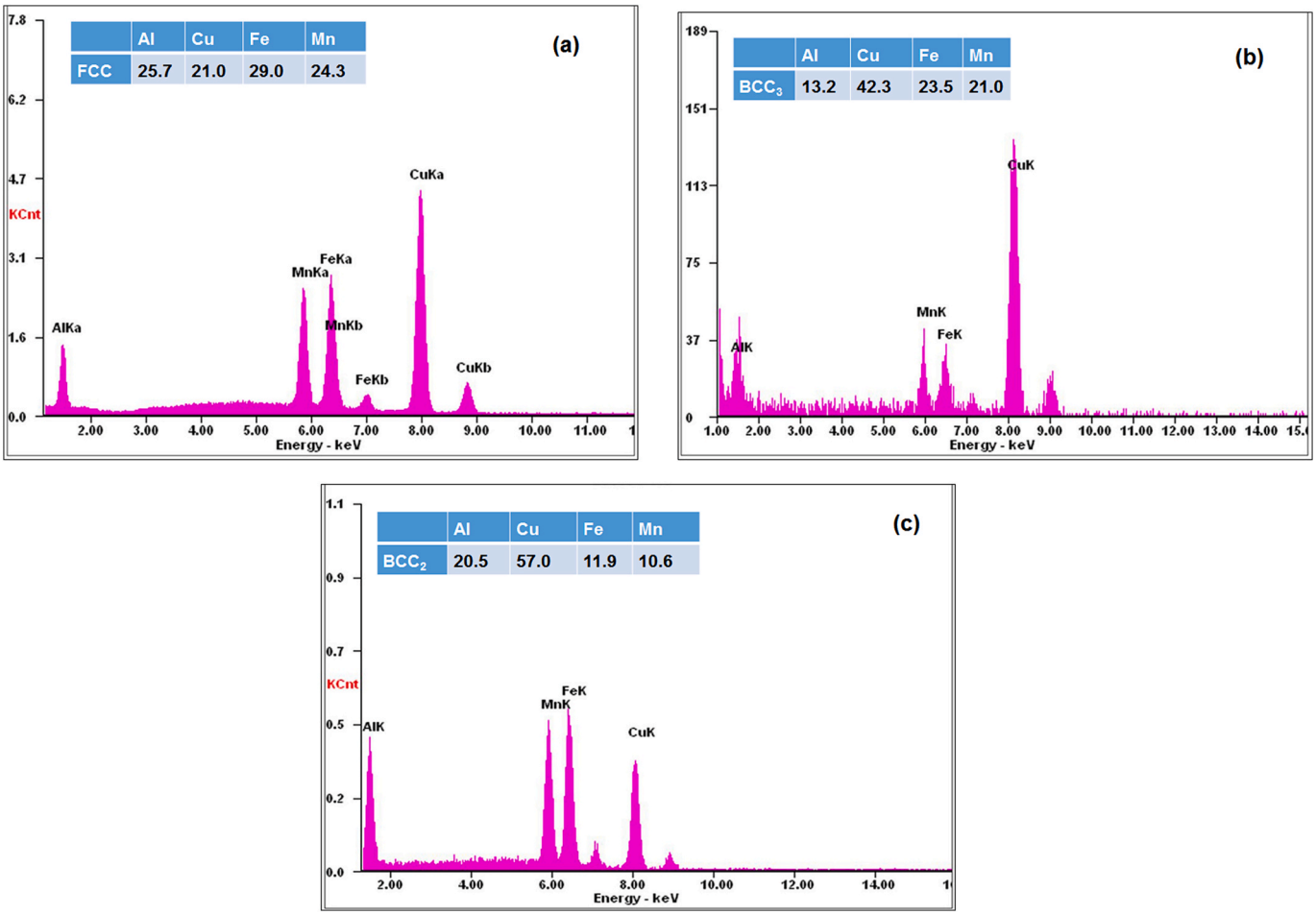

Fig. 6. Representative EDS spectrum of FCC, BCC_2 and BCC_3 phases (shown in Fig. 5) obtained from TEM. In inset, typical median composition of the phases is provided.

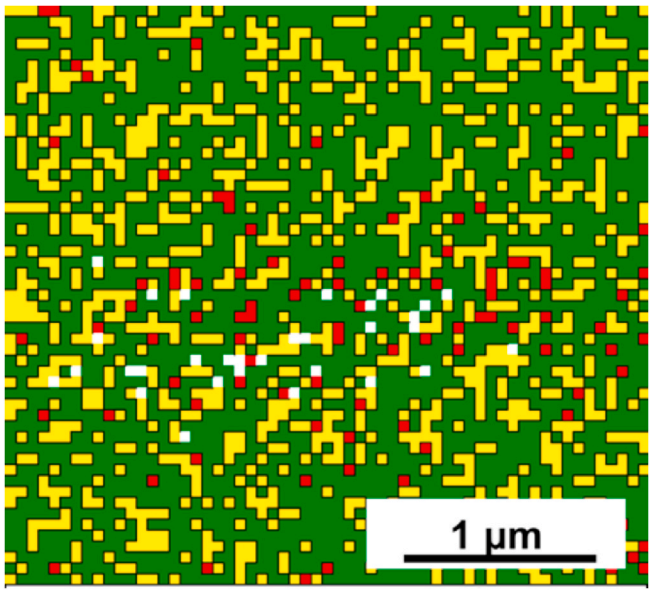

Fig. 7. Typical phase-contrast map of the alloy, where green denotes the FCC phase, while yellow is the BCC_2 phase, and red is the BCC_1 phase. The white regions indicate positions where Kikuchi patterns are unresolved. The mapping was done at a step size of 60 nm. (For interpretation of the references to colour in this figure legend, the reader is referred to the Web version of this article.)

3. Results

3.1. Composition and microstructure

The cross-sectional microstructure of the arc-melted alloy button displays columnar structures as observed in the Euler orientation map obtained using EBSD (Fig. 1). EDS of individual columnar grains indicates localized elemental partitioning into iron-rich - Region 1 and copper-rich - Region 2 (Fig. 2). The average composition of Regions 1 and 2 is given in Table 1. The high-resolution SEM image of Region 1 exhibits a cuboidal phase dispersed in a sparse matrix while Region 2 reveals an interweaved structure (Fig. 3). Besides this, a mixed morphology consisting of both cuboidal and interweaved structures is also observed. In Fig. 4, the X-ray diffraction pattern of the alloy is presented where peaks typical of body-centered cubic (BCC) and face-centered cubic (FCC) crystal structures are observed. The corresponding lattice parameter of the FCC phase is 5.85 ± 0.01 Å while that of the two BCC phases are of 5.11 ± 0.01 Å (BCC_1) and 2.93 ± 0.01 Å (BCC_2) respectively. High-resolution electron backscattered diffraction mapping further confirmed the presence of three phases (Fig. 7) where FCC adjoins the BCC_2 phase, while BCC_1 is sparsely distributed.

Detailed microstructure and phase analysis using TEM revealed that Region-1 comprised of clustered cuboid phases (Fig. 5- marked by yellow arrows) of size less than 40 nm with an FCC structure (a ≈5.85 Å) in addition to tiny (less than 15 nm) isolated BCC_3 (a ≈5.93 Å) phase. In Region-2 an interlaced structure consisting of stringer (long and or short) aggregates of BCC crystal structure with a lattice parameter of ~2.4 Å (Fig. 5) exists, which corresponds to the BCC_2 phase in the pXRD

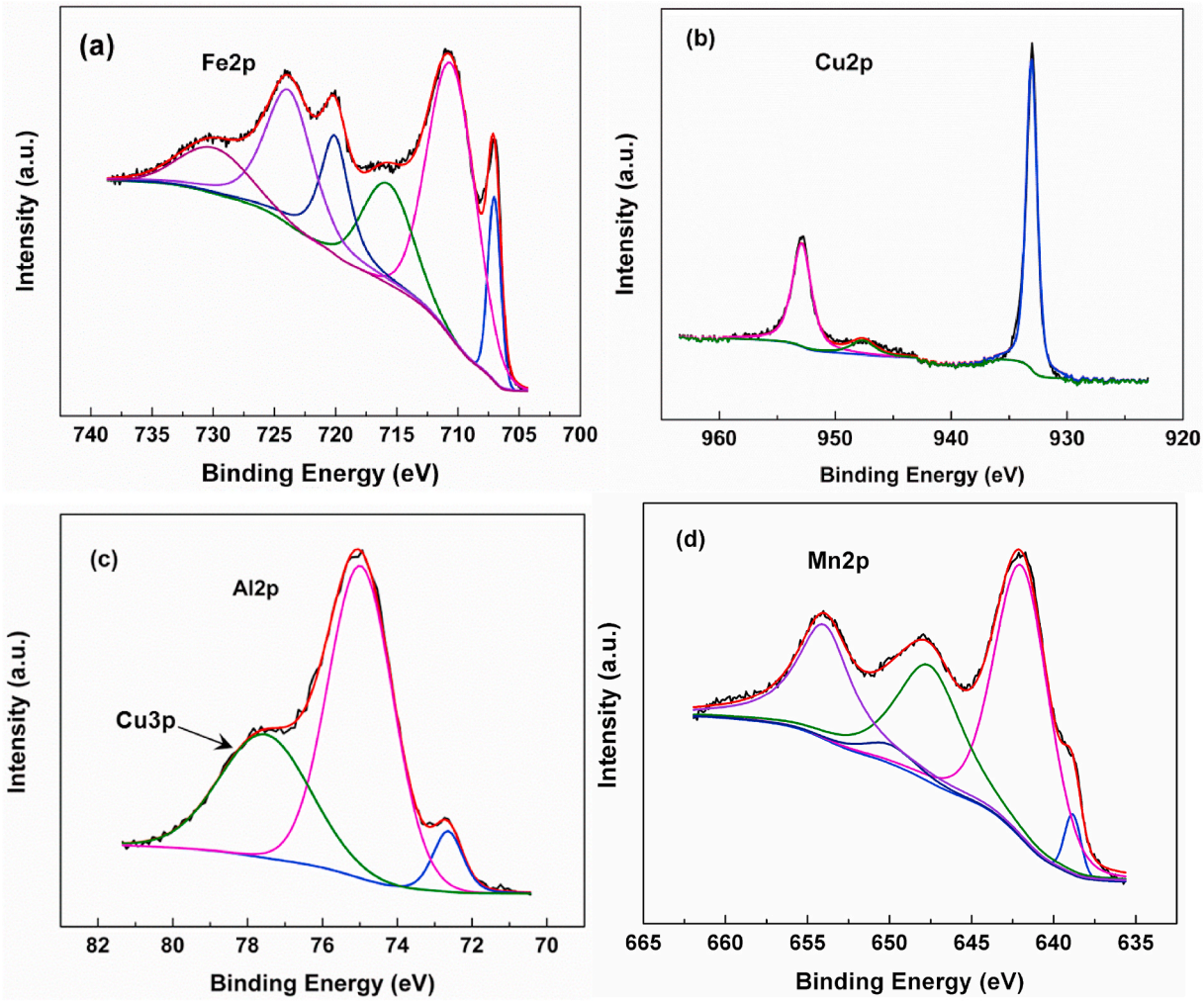

Fig. 8. XPS spectra of Fe2p, Cu2p, Al2p and Mn2p levels in as prepared AlCuFeMn alloy.

pattern. The cuboidal FCC phase in Region-1 corresponds to the FCC phase in the pXRD pattern (Fig. 4). However, BCC_3 phase (a ≈5.93 Å) is not evident in the pXRD pattern and is possibly due to its sparse distribution. The BCC_1 peaks in pXRD pattern are inferred to be that of the continuous matrix present in Region 1 and 2 respectively. In Fig. 6, characteristic X-ray spectrum obtained from EDS and corresponding semi-quantitative composition of FCC, BCC_2 and BCC_3 phase are presented. Similar EDS analysis of the stainless steel sample indicates a typical AISI 304 composition and is presented in Table −1.

3.2. X-ray photoelectron spectroscopy

Figs. 8 and 9 illustrate the XPS spectrums of AlCuFeMn alloy for **Sample A** (as-cast) and **Sample B** (surface-oxidized) specimens. In **Sample A**, iron (Fig. 8(a)) is present in both metallic and oxidized state with B.E. peaks at 706.6 eV and 710.1 eV corresponding to the metallic and oxide of $Fe2p_{3/2}$ level, respectively. The satellite peak (at 716 eV) also indicates that Fe is present mostly in the Fe^{2+} state. In **Sample B** (Fig. 9(a)), the metallic peak vanishes and iron is in its complete oxide state. The oxide peak at B.E. 710.1 eV and 712.4 eV and their satellite peaks around 716 eV and 720 eV are primarily attributed to Fe(II) state and Fe(III) state, respectively.

For Cu, two peaks appear for **Sample A** at 932.5 eV (2p3/2) and 952.3 eV (2p1/2) suggesting metallic Cu while a weak satellite around 947 eV suggests the presence of Cu (I) state (Fig. 8(b)). In **Sample B**, the 2p3 peaks broaden with an increase in the satellite peak, suggesting an increase in the Cu (I) state (Fig. 9(b)). The Cu LMM Auger spectra of the surface-oxidized samples (not shown) suggest that Cu is present in both metallic and Cu (I) state.

For **Sample A**, Al peaks are observed at binding energies 72.2 eV and 74.5 eV (Fig. 8(c)) corresponding to the metallic and oxide state of Al $2p_{3/2}$, respectively. While in **Sample B** (Fig. 9(c)) Al is in a completely oxidized state. The peak at 77 eV in the spectrum corresponds to Cu3p level.

For manganese (Fig. 8(d)), peaks at 638.5 eV and 641.5 eV corresponds to the metallic and oxidized state of Mn2p. The broad peak at 647.6 eV corresponds to the Auger peak of Cu LMM. For **Sample B**, manganese present is in a completely oxidized state (Fig. 9(d)).

3.3. Potentiodynamic polarization

Fig. 10(a) presents the linear polarization curves of AISI 304 stainless steel, **Sample A,** and **Sample B** in 3.5 wt % aqueous NaCl solution. The measured values of the electrochemical parameters summarized in Table 2 indicate that AISI 304 (density 7.90 g/cm^3) [14] is nobler compared to the others. The corrosion current density (i_{corr}) is measured from the Tafel plot by extrapolating the linear portion of the polarization curve near corrosion potential (E_{corr}) as shown in Fig. 10(b–d). The anodic (β_a) and cathodic (β_c) Tafel constants are measured from the slopes of the anodic and cathodic branches, respectively. The E_{corr} and i_{corr} values obtained for AISI 304 are very similar to the results observed in Ref. [14] (−250 mV_{SCE} and 0.601 μA/cm^2, respectively). The

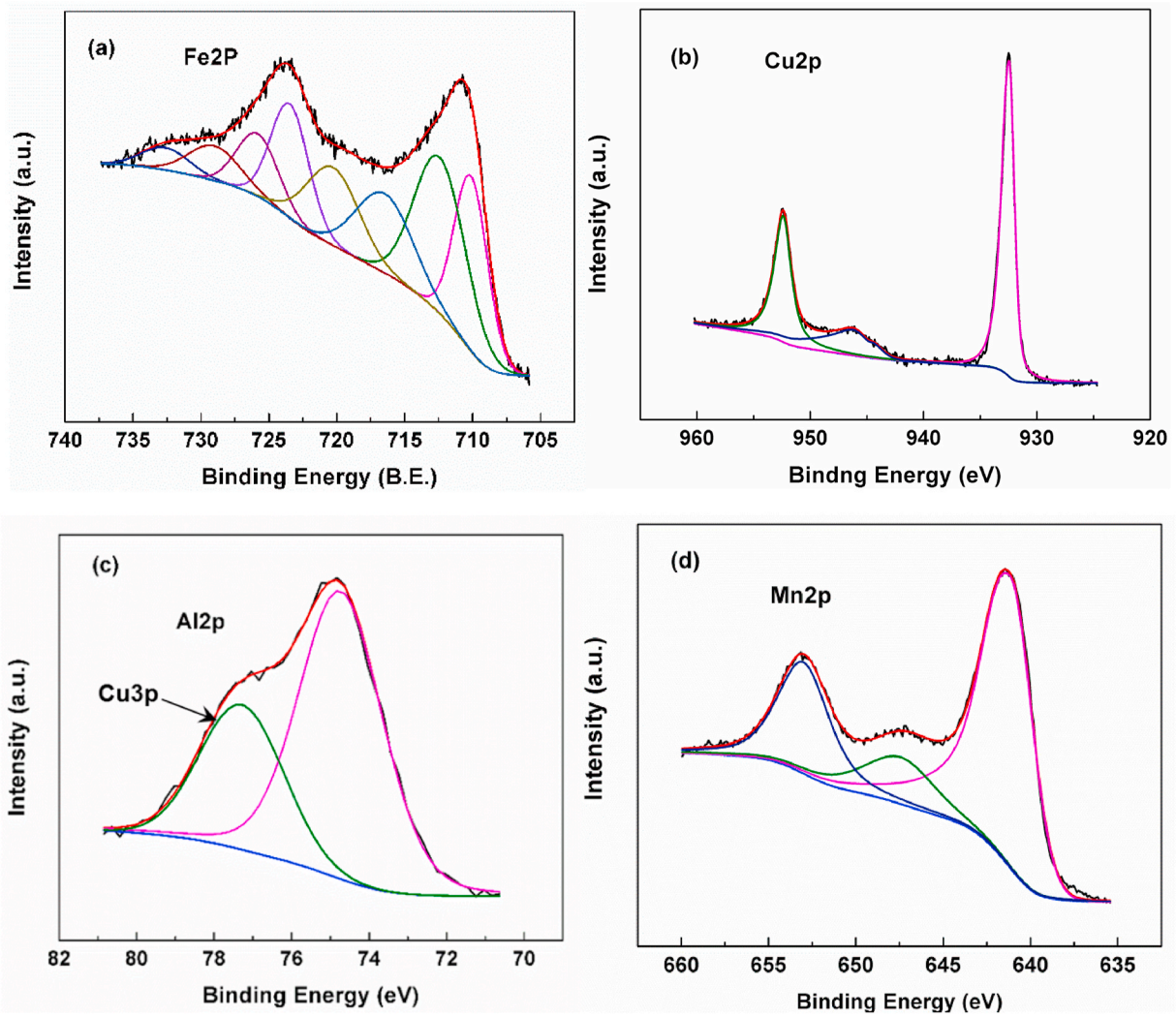

Fig. 9. XPS spectra of Fe2p, Cu2p, Al2p and Mn2p levels in air-oxidized AlCuFeMn alloy.

corrosion rate (r_{corr}) of the alloys are calculated according to Faraday's law as [5].

$$r_{corr} = 0.00327 \frac{i_{corr} \times EW}{D} = 0.00327 \frac{i_{corr}}{D \sum \left(\frac{f_i n_i}{a_i} \right)} \text{(mm / yr)} \quad (1)$$

where i_{corr} is the corrosion current density (μA/cm^2), D is mass density (g/cm^3), f_i is mass fraction, a_i is atomic weight (at.%) and n_i is the number of equivalents exchanged. The equivalent weight (EW) of AlCuFeMn alloy being ~18.62 and that of AISI 304–28, respectively. The calculated corrosion rate of **Sample A** in 3.5 wt% aqueous NaCl is 0.034 mmpy, compared to 0.009 mmpy for AISI 304 and illustrates no passivation. In contrast, **Sample B** exhibits passivation and metastable pitting manifested by a fluctuating corrosion current with an overall improvement in OCP and a corrosion rate similar to AISI 304. The passivation region fails at the critical pitting potential (E_{pit} in Fig. 10(c)) enhancing the corrosion rate.

3.4. Electrochemical impedance spectroscopy

The Nyquist and Bode plots of **Sample A & B** in 3.5 wt% NaCl solution are shown in Fig. 11(a–c) and Fig. 12(a–c). The Nyquist plots contain two capacitive arcs, typical of metal-oxide (M/O) and oxide-electrolyte interface (O/E) at high and low-frequency regions [15]. In all the plots a good fit between experimental and simulated data is observed. The electrical equivalent circuit used to obtain the simulated spectra in both cases is presented in Fig. 11(d). The circuit consists of two parallel RQ arrangements with the solution resistance (R_S) in series while R_{pit} is the resistance of solution inside the pit and CPE_{pit} is the pit wall capacitance [15]. Similarly, R_P and CPE_P are corresponding parameters associated with the passive layer [15].

It may be noted that considering surface inhomogeneities, surface roughness, and composition variation of surface layers, a Constant Phase Element (CPE or Q) instead of a pure capacitor (C) is used [16]. The CPE impedance (Z_{CPE}) being given by [17].

$$Z_{CPE} = Y_0^{-1} (j\omega)^{-n} \quad (2)$$

where Y_0 is the proportionality factor, j is the imaginary unit, ω is angular frequency and n is the phase shift. The values for corresponding circuit components of both samples are summarized in Table 3.

In Fig. 13, a typical scanning electron micrograph of the specimen surface after 48 h of immersion is presented. The micrograph shows irregularly shaped pits which supports the potentiodynamic test results and the EIS model for corrosion.

3.5. EDS analysis

In Fig. 14, the elemental distribution at surface of **Sample A** after corrosion is presented. The EDS results indicate uniform elemental distribution with a thin visible oxide layer formation. In Fig. 15, the EDS

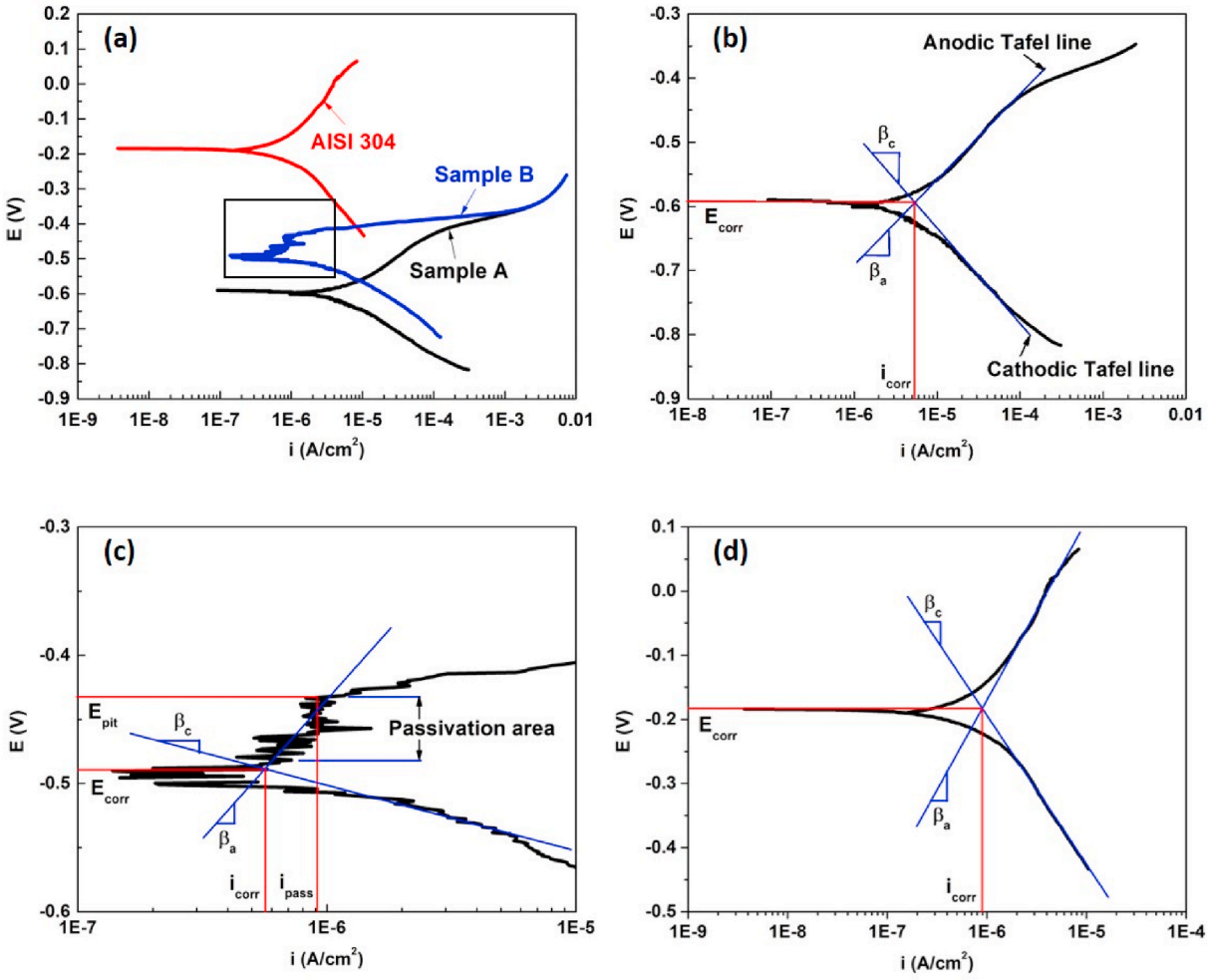

Fig. 10. Potentiodynamic polarization curves for (a) AISI 304 and AlCuFeMn alloys in a 3.5% NaCl solution. Anodic and Cathodic Tafel lines showing corrosion potential and corrosion current density in (b) Sample A, (c) Sample B (enlarged passivation region), and (d) AISI 304.

Table 2
Electrochemical parameters of the AlCuFeMn alloys in a 3.5% NaCl solution.

	D (g/cm^3)	E_{corr} (mV vs. SCE)	i_{corr} (μA/cm^2)	r_{corr} (mmpy)
Sample A (as-cast)	6.53	−596.24	5.322	0.049
Sample B (air-oxidized)	6.53	−488.86	0.561	0.004
AISI 304	7.90	−180	0.86	0.009

map of a typical corroded cross-section of **Sample B** after EIS is presented. The corroded surface consists of an oxide layer which is few microns in thickness and is predominantly of copper with minor presence of iron, aluminum and manganese.

4. Discussion

The microstructure of AlCuFeMn alloy consists of columnar arrangements typical of dendritic solidification (Fig. 1). Within the grains, iron-rich cuboidal Region 1, threaded copper-rich Region 2 and a mixed morphology region exist. This phase morphology is similar to that reported by Roy et al. [6] except for the absence of the mixed region. It is to be noted that the cast AlCuFeMn sample investigated by Roy et al. [6] was annealed for 80 h at 500 °C, unlike the as-cast state used in this work. However, the principal phases obtained from the present pXRD data (Fig. 4) corresponds with that of Roy et al. [6] where a mixture of FCC phase with lattice parameter 5.85 Å (iron-rich cuboidal Region 1) and BCC_2 phase (copper-rich threaded Region 2) of 2.93 Å were reported. The phases were further confirmed during TEM analysis and EBSD mapping as shown in Figs. 5 and 7. The FCC phase located in Region 1 (see Reference [6]) is remarkably similar to the FCC intermetallic phase Fe_3Al with a lattice parameter of 5.65 Å [18]. However, the BCC_2 phase and the additional BCC_1 phase reported in this work are unlike any equilibrium Fe-Al binary intermetallic compounds. The BCC_1 and BCC_3 phases were not reported by Roy et al. [6] and had a minor volume fraction compared to the principal phases.

The corrosion resistance of as-cast AlCuFeMn alloy i.e., **Sample A** ($i_{corr} \sim 5.322$ μA/cm^2) in aqueous 3.5% NaCl solution is lower than as-cast CoCrFeMnNi which has an i_{corr} of 0.38 μA/cm^2 [3]. However, the resistance improved substantially after surface oxidation (**Sample B**) and became comparable to AISI 304 steel [3]. The results indicate that protective surface layer development plays an important role in the aqueous corrosion protection of AlCuFeMn alloy. Significantly, potentiodynamic polarization curve of **Sample B** demonstrated serrations below E_{pit} which is attributed to pit nucleation, growth, and repassivation typical of metastable pitting [19,20]. On the other hand, the

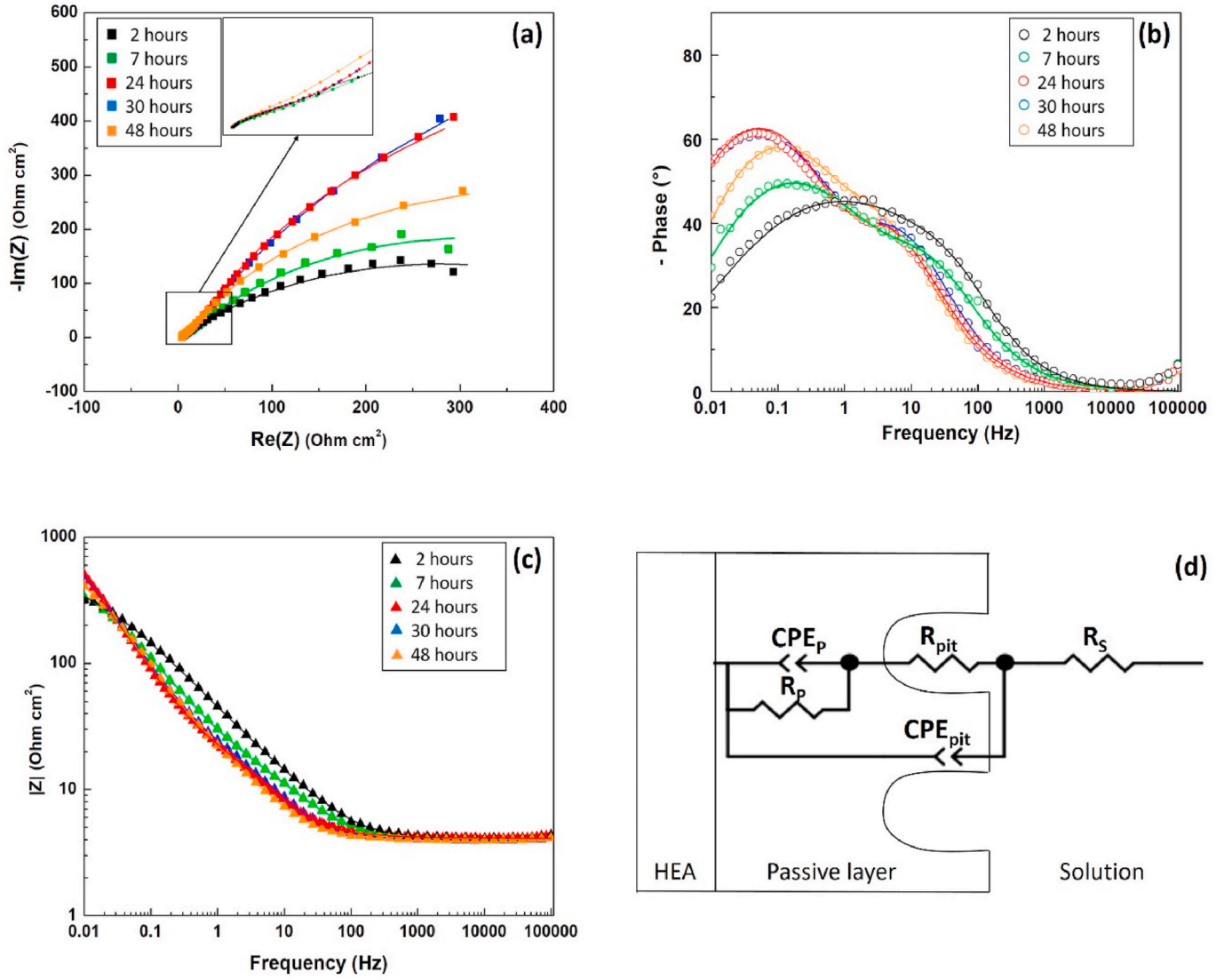

Fig. 11. Nyquist (a) and Bode phase (b) and Bode modulus (c) plots for as-cast AlCuFeMn alloy after 2, 7, 24, 30 and 48 h of immersion in 3.5 wt% NaCl solution. Equivalent circuit used to analyze the EIS results (d).

polarization curve of the as-cast alloy (Fig. 10) demonstrates an absence of distinct passivation and propensity to pitting corrosion similar to cast CoCrFeMnNi alloy [3]. The pitting corrosion susceptibility of CoCrFeMnNi alloy in 3.5 wt% NaCl solution was ascribed to microsegregation of chromium (dendritic region) and nickel (interdendriditic region) [3] respectively. Quite similarly, pitting corrosion in the as-cast alloy (**Sample A**) is attributable to separation of copper into BCC_2 phase (Region-2) and iron in the FCC phase (Region-1). Alternatively, in **Sample B**, the oxide layer formation on the other hand results in a passivation tendency with resultant metastable pitting. The above pitting behavior difference correlates well with the equivalent circuits obtained from the EIS study, where simultaneously (a) pitting due to local alkalization and (b) growth and deterioration of the passive layer is observed. For any alloy, an "n" value between 0.5 and 0.8 of CPE indicates a deviation from ideal capacitor behavior and is attributed to the formation of an inhomogeneous corroded surface [16]. Thus, the increase in R_P value for the first 30 h of immersion (Table 3) in **Sample A,** reflects the formation and development of a protective layer [21]. Thereafter, R_P value decreases from 1849.1 Ω cm^2 to 763.2 Ω cm^2, implying localized damage to the protective film [22]. Once the protective layer breaks down, it doesn't regenerate immediately. The damaged regions are consequently attacked by chloride ions (Cl^-) in solution, resulting in galvanic cell formation, pit creation and propagation [19]. Further increase in pit resistance (R_{pit}) with exposure time, indicates decreased pit growth rate [23]. Consequently, R_{pit} decreases at 30 h but reverts to a maximum value at 48 h suggesting an insignificant increase in active surface within the pits [24,25]. On the other hand, in **Sample B** (oxidized surface condition) the initial R_P values are considerably higher and comparable to 24 h value for **Sample A**. The observation indicates that the protective layer formed during low-temperature oxidation acts as an effective barrier to metal ion transport immediately after immersion. Thus, the consistently high R_{pit} value of **Sample B** compared to **Sample A** indicates a better pitting corrosion resistance. According to the Helmholtz model [26], the thickness of any passive layer is

$$\delta = \frac{\varepsilon_0 \varepsilon}{Y_0} S \tag{3}$$

where ε_0 is permittivity of free space (8.85×10^{-14} F/cm), ε is the dielectric constant of the medium and S is the surface area of the electrode. As seen in Table 3, the Y_0 value for the protective layer on **Sample B** is significantly smaller in comparison to **Sample A**. This suggests improved protection by the superficial oxide layer in the surface oxidized specimen compared to as-cast [22].

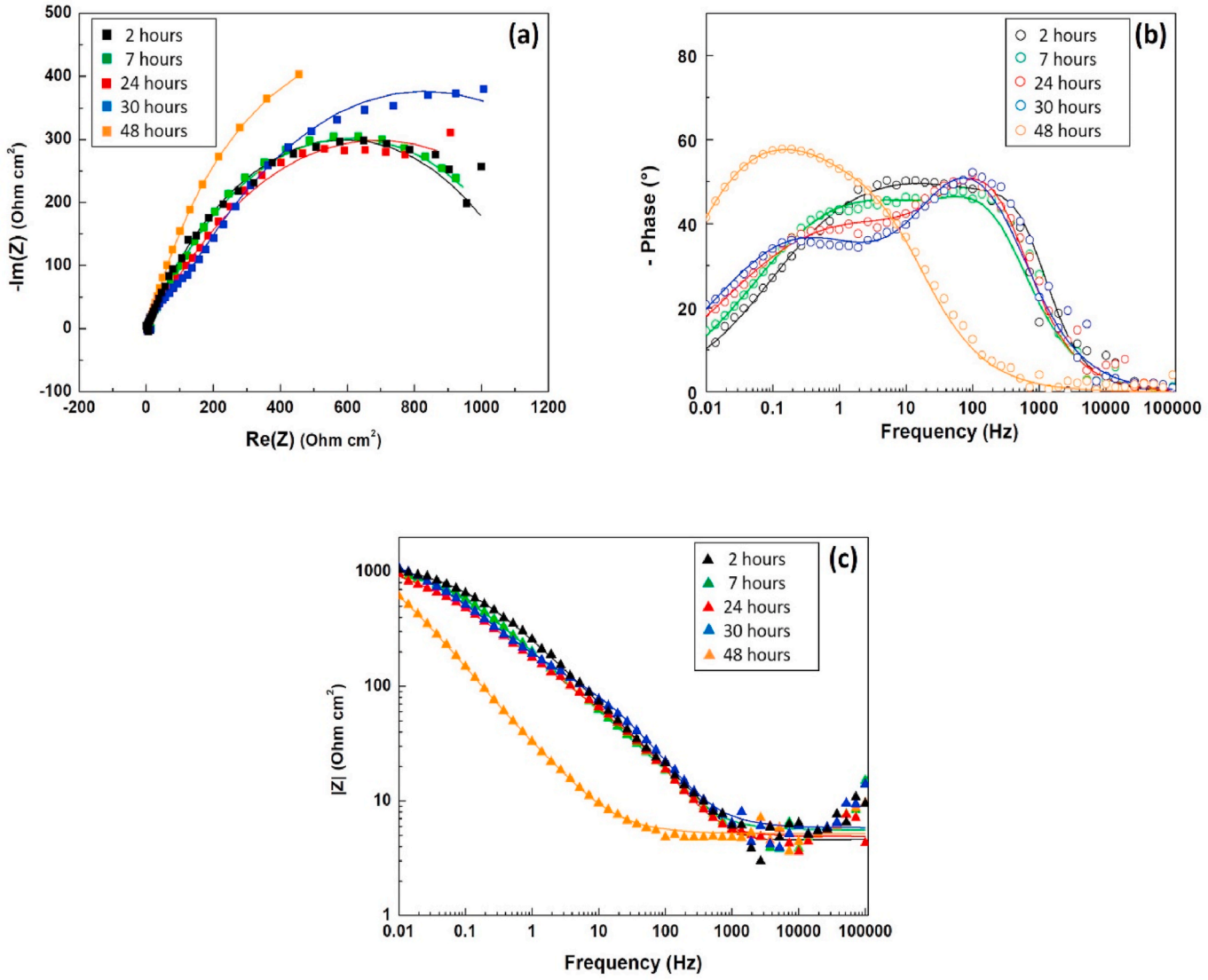

Fig. 12. Nyquist (a) and Bode phase (b) and Bode modulus (c) plots for air-oxidized AlCuFeMn alloy after 2, 7, 24, 30 and 48 h of immersion in 3.5 wt% NaCl solution.

Table 3
EIS results for as-cast and air-oxidized AlCuFeMn medium entropy alloys after different immersion times.

Sample	Immersion time	R_S (Ω cm^2)	R_{pit} (Ω cm^2)	R_P (Ω cm^2)	CPE_{pit}		CPE_P	
					Y_{01}(μΩ^{-1} cm^{-2} S^{-n})	n_1	Y_{02}(μΩ^{-1} cm^{-2} S^{-n})	n_2
As-cast	2 h	4.10	10.8	554.7	1838.2	0.809	6543.7	0.543
	7 h	4.05	17.9	603.5	3973.8	0.754	8685.3	0.665
	24 h	4.11	36.5	1502.8	7971.4	0.749	9101.7	0.860
	30 h	3.98	27.1	1849.1	5883.4	0.781	9875.1	0.778
	48 h	3.98	40.1	763.2	8982.7	0.760	6424.7	0.795
Air-oxidized	2 h	5.44	31.8	1173.3	1154.1	0.596	175.2	0.824
	7 h	5.59	34.1	1182.4	1475.3	0.571	205.9	0.863
	24 h	4.92	35.1	1330.5	2076.1	0.525	137.0	0.918
	30 h	5.83	98.2	1494.1	2201.1	0.573	241.7	0.821
	48 h	5.19	74.1	1259.2	3402.7	0.696	651.1	0.769

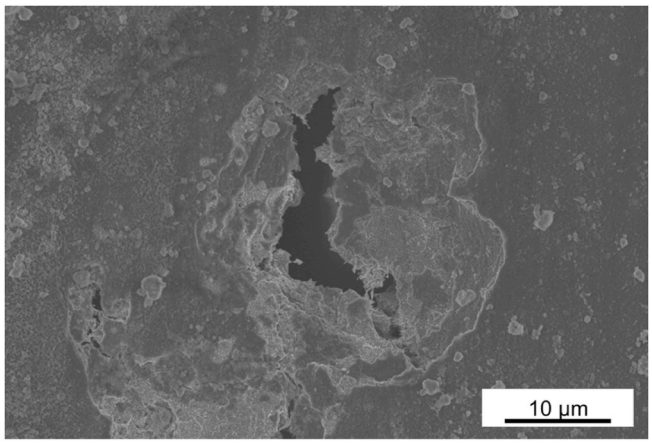

Fig. 13. SEM images of the corroded surface with pit formation after 48 h EIS test in 3.5 wt% NaCl solution.

The above corrosion behavior is further elucidated using the EDS and XPS results. The EDS cross-sectional analysis of **Sample A** indicates an oxygen enriched surface with all four elements unlike the pronounced copper enriched oxide layer in **Sample B**. The result corresponds to the XPS results of the as-cast sample surface before corrosion where all the four elements are in an oxidized state, along with a small fraction in the metallic form. Moreover the elemental iron is in multiple oxidation states. Passivation offered by such mixed oxide films along with lower valence oxides is poor [27–29]. Thus, the protective layer in the as-cast alloy (**Sample A**), with extant metal is both ionically and electronically conductive resulting in diminished corrosion resistance in a 3.5 wt % NaCl aqueous solution.

On the other hand, the surface oxidized alloy (**Sample B**) displays a brief passivation with metastable pitting followed by a transpassive region of pit growth. The results correlates with the XPS spectra of the surface oxidized sample in Fig. 9 where the metallic states present in the as-cast specimen reduces (in case of Cu) or completely disappears (in the case of Fe, Al, and Mn). This improves the barrier protection offered by the oxide layer in **Sample B** compared to **Sample A** [27–29]. Similar enhancement in aqueous corrosion resistance of ternary chromium alloyed Fe_3Al intermetallics is ascribed to the formation of the p-type passive layer due to Cr^{3+} and Cr^{6+} enrichment [30]. However, such passive layer formation cannot completely resist pitting corrosion in a chloride environment [30].

Again, failure of corrosion resistance for **Sample B** at E_{pit} can be explained from the nature of the protective surface layer observed in post corrosion cross-section of **Sample B** (see Fig. 15)**,** where a layer of copper oxide, with minor presence of aluminum, iron, and manganese is seen. It is to be noted that, XPS results before corrosion (Fig. 9) indicated presence of all elements on the surface in an oxidized state. This suggests a preferential dissolution of elements from the protective oxide layer during corrosion resulting in the ultimate failure of the passivation process in **Sample B** beyond ~ (−)0.43 V (Fig. 10). However, a more in-depth study is required to understand the mechanism of this failure and is the subject of future work.

5. Conclusions

The microstructure of as-cast AlCuFeMn alloy is similar to that of cast-annealed AlCuFeMn reported earlier by Roy et al. [6] apart from the two additional minor phases. The corrosion resistance of the surface oxidized alloy (at 473 K) in 3.5 wt% aqueous NaCl is similar to stainless steel although the as-cast sample shows a higher corrosion rate. Pitting corrosion tendency observed in the as-cast state improved after low-temperature oxidation due to complete oxidation of Al, Fe, and Mn atoms. However, the pitting resistance failed beyond ~ −0.43 V due to the selective dissolution of the protective layer. Overall, the aqueous corrosion resistance of the AlCuFeMn alloy in 3.5 wt% NaCl solution is comparable to corrosion resistant HEA like CoCrFeMnNi and is significantly superior to that of binary iron aluminides reported in literature.

CRediT authorship contribution statement

A. Dutta: Investigation, Writing – original draft, Writing – review & editing, Formal analysis. **T. Sivaji:** Investigation. **M. Ghosh:** Investigation, Writing – review & editing, Data curation, Formal analysis. **R. Fernandes:** Investigation, Writing – review & editing, Data curation, Formal analysis. **P.S. De:** Conceptualization, Methodology, Investigation, Writing – review & editing, Supervision, Data curation, Formal analysis. **D. Nayak:** Validation, Writing – review & editing. **R. Sharma:**

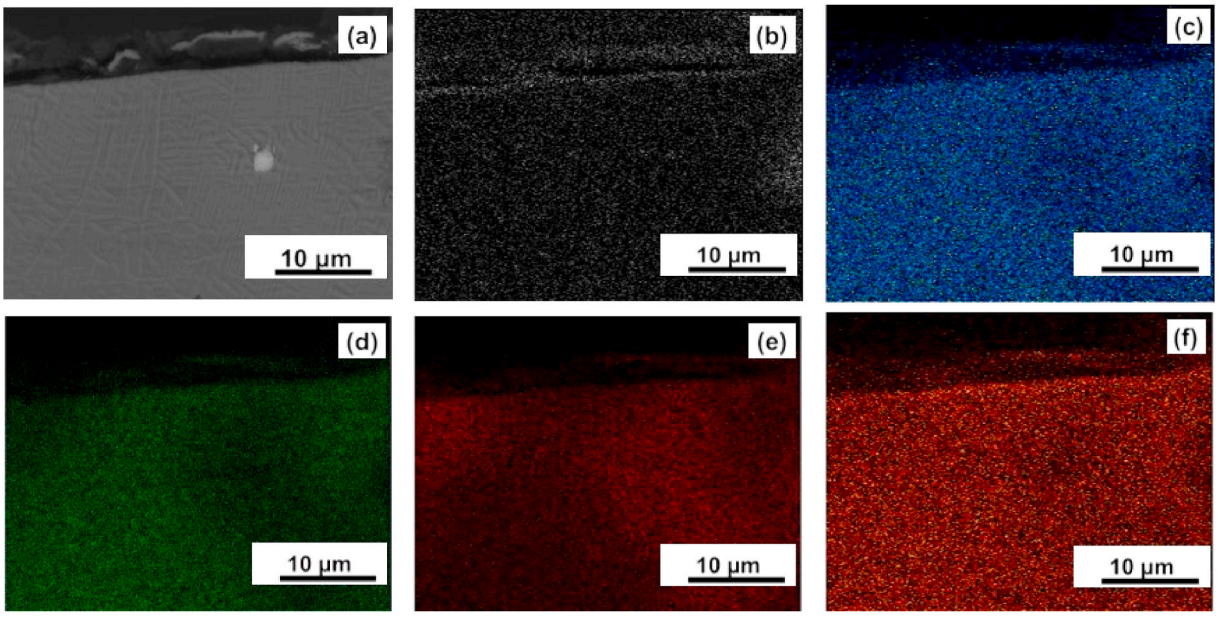

Fig. 14. EDS image of the cross-section of **Sample A** (as-cast) after potentiodynamic polarization, showing (a) Electron Image (b) Oxygen distribution (c) Manganese distribution (d) Iron distribution (e) Copper distribution and (f) Aluminum distribution.

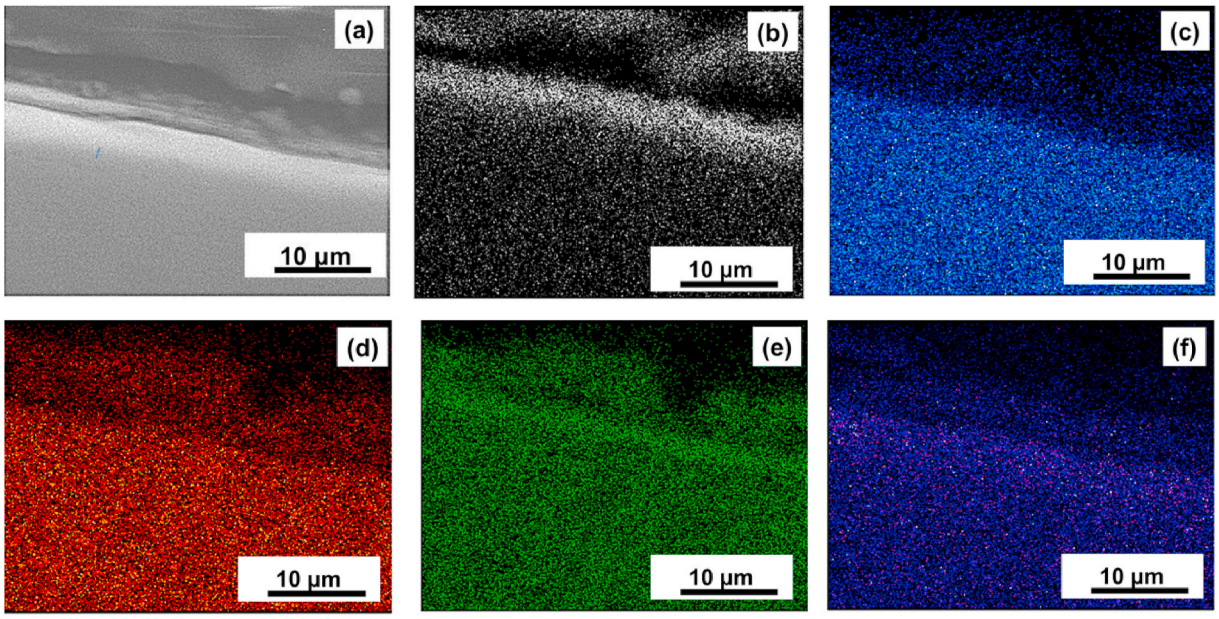

Fig. 15. EDS image of the cross-section of Sample B (cast and oxidized at 200 °C) after EIS, showing (a) Electron Image (b) Oxygen distribution (c) Manganese distribution (d) Iron distribution (e) Copper distribution and (f) Aluminum distribution.

Investigation.

Declaration of competing interest

The authors declare that they have no known competing financial interests or personal relationships that could have appeared to influence the work reported in this paper.

Acknowledgement

One of the authors (PSD) would like to acknowledge the assistance of Mr. Lokanath Sathua, scientific assistant at IIT Bhubaneswar, for his help in conducting the SEM and EBSD experiments.

References

[1] M.-H. Tsai, J.-W. Yeh, High-entropy alloys: a critical review, Mater. Res. Lett. 2 (2014) 107–123.
[2] Y. Zhang, et al., Microstructures and properties of high-entropy alloys, Prog. Mater. Sci. 61 (2014) 1–93.
[3] S. Pathak, N. Kumar, R.S. Mishra, P.S. De, Aqueous corrosion behavior of cast CoCrFeMnNi alloy, J. Mater. Eng. Perform. 28 (2019) 5970–5977.
[4] C.L. Wu, S. Zhang, C. Zhang, H. Zhang, S. Dong, Phase evolution and cavitation erosion-corrosion behavior of FeCoCrAlNiTix high entropy alloy coatings on 304 stainless steel by laser surface alloying, J. Alloys Compd. 698 (2017) 761–770.
[5] Y.Y. Chen, T. Duval, U.D. Hung, J.W. Yeh, H.C. Shih, Microstructure and electrochemical properties of high entropy alloys — a comparison with type-304 stainless steel, Corrosion Sci. 47 (2005) 2257–2279.
[6] A. Roy, M. Ghosh, H. Gourkar, P.S. De, Microstructure, indentation and first principles study of AlCuFeMn alloy, Materialia 5 (2019), 100206.
[7] R. Sharma, A. Roy, P.S. De, Equimolar AlCuFeMn: a novel oxidation resistant alloy, Intermetallics 135 (2021), 107215.
[8] R. Prescott, M.J. Graham, The oxidation of iron-aluminum alloys, Oxid. Metals 38 (1) (1992) 73–87.
[9] C.T. Liu, C.G. McKamey, E.H. Lee, Environmental effects on room-temperature ductility and fracture in Fe_3Al, Scr. Metall. 24 (2) (1990) 385–389.
[10] C.T. Liu, E.H. Lee, C.G. McKamey, An environmental effect as the major cause for room-temperature embrittlement in FeAl, Scr. Metall. 23 (6) (1989) 875–880.
[11] M.C. García-Alonso, M.F. López, M.L. Escudero, J.L. González-Carrasco, D. G. Morris, Corrosion behaviour of an Fe_3Al -type intermetallic in a chloride solution, Intermetallics 7 (1999) 185–191.
[12] ASTM G61-86, Standard Test Method for Conducting Cyclic Potentiodynamic Polarization Measurements for Localized Corrosion Susceptibility of Iron-, Nickel-, or Cobalt-Based Alloys, 2018.
[13] Y.P. Sun, Z. Wang, H.J. Yang, A.D. Lan, J.W. Qiao, Effects of the element La on the corrosion properties of CrMnFeNi high entropy alloys, J. Alloys Compd. 842 (2020) 1–10.
[14] Y. Hsu, W. Chiang, J. Wu, Corrosion behavior of FeCoNiCrCu x high-entropy alloys in 3 . 5 % sodium chloride solution, Mater. Chem. Phys. 92 (2005) 112–117.
[15] A. Aballe, M. Bethencourt, F.J. Botana, J. Cano, M. Marcos, EIS study of the electrochemical response of AA5083 alloy under anodic polarisation, Corros. Rev. 18 (2000) 1–9.
[16] L.M. Calle, M.R. Kolody, R.D. Vinje, M.C. Whitten, W. Li, Electrochemical impedance spectroscopy of alloys in a simulated space shuttle launch environment, Eurocorr (2005) 1–11. September 04, 2005 - September 08, 2005; Lisbon; Portugal.
[17] G.S. Peng, K.H. Chen, H.C. Fang, H. Chao, S.Y. Chen, EIS study on pitting corrosion of 7150 aluminum alloy in sodium chloride and hydrochloric acid solution, Mater. Corros. 6 (9) (2010) 783–789.
[18] R. Mitra, Structural Intermetallics and Intermetallic Matrix Composites, CRC Press, Boca Raton, Florida, USA, 2015.
[19] G.S. Frankel, Pitting corrosion of metals A review of the critical factors, J. Electrochem. Soc. 145 (6) (1998) 2186–2198.
[20] H. Kaesche, Microtunnelling during selective alloy dissolution and during pitting, Werkstoffe Korrosion 39 (1988) 152.
[21] M. Galai, H. Benqlilou, M.E. Touhami, T. Belhaj, K. Berrami, H.E. Kafssaoui, Comparative analysis for the corrosion susceptibility of copper alloys in sandy soil, J. Appl. Electrochem. 39 (10) (2009) 1725–1731.
[22] Q. Ye, et al., Microstructure and corrosion properties of CrMnFeCoNi high entropy alloy coating, Appl. Surf. Sci. 396 (2017) 1420–1426.
[23] F. Mansfeld, F. Huet, O.R. Mattos, New trends in electrochemical impedance spectroscopy (EIS) and electrochemical noise analysis (ENA), Proc. Int. Sympos. 2000-24 (2001).
[24] J.R. Scully, D.C. Silverman, Electrochemical Impedance: Analysis and Interpretation, ASTM International, 1993.
[25] K. Jafarzadeh, T. Shahrabi, A.A. Oskouei, Novel approach using EIS to study flow accelerated pitting corrosion of AA5083-H321 aluminum-magnesium alloy in NaCl solution, J. Appl. Electrochem. 39 (10) (2009) 1725–1731.
[26] C.F. Zinola, A.M.C. Luna, The inhibition of Ni corrosion in H2SO4 solutions containing simple non-saturated substances, Corrosion Sci. 37 (12) (1995) 1919–1929.
[27] F.P. Fehlner, N.F. Mott, Low temperature oxidation, Oxid. Metals 2 (1970) 59–99.
[28] J.S. Leach, B.R. Pearson, Crystallization in anodic oxide films, Corrosion Sci. 28 (1988) 43–56.
[29] T.L. Barr, An ESCA study of the termination of the passivation of elemental metals, J. Phys. Chem. 82 (1978) 1801–1810.
[30] M. Zamanzade, A. Barnous, Effect of chromium on the electrochemical properties of iron aluminide intermetallics, Corrosion Sci. 78 (2014) 223–232.